Supporting Information

Interfacial coordination utilizing chelating ligands for operationally stable perovskite solar modules

Author list: Bingkun Tian[1, //], Peikun Zhang[1, //], Tianjun Liu[2, //], Weicun Chu[1], Yuyang Long[1], Peng Xu[1], Ying Jiang[1], Jinping Zhang[1], Yajing Tang[1], Xiangnan Sun[1], Riming Nie[1], Xiaoming Zhao[1,*], Wanlin Guo[1,*] and Zhuhua Zhang[1,*]

Affiliations:

[1] State Key Laboratory of Mechanics and Control for Aerospace Structures, Key Laboratory for Intelligent Nano Materials and Devices of Ministry of Education, and Institute for Frontier Science, Nanjing University of Aeronautics and Astronautics, Nanjing 210016, China

[2] Cavendish Laboratory, Department of Physics, University of Cambridge, Cambridge CB3 0HE, UK.

*Correspondence to: Xiaoming Zhao (Email: xiaoming.zhao@nuaa.edu.cn), Wanlin Guo (Email: wlguo@nuaa.edu.cn) and Zhuhua Zhang (Email: chuwazhang@nuaa.edu.cn)

// Bingkun Tian, Peikun Zhang and Tianjun Liu contributed equally to this work.

Experimental Section

Materials: N,N'-di(4-pyridyl)-1,4,5,8-naphthalenetetracarboxdiimide （DPNDI） and 2,7-Diphenylbenzo [lmn][3,8]phenanthroline-1,3,6,8 (2H ,7H)-tetraone (DBNDI) were purchased from Sigma-Aldrich. MACl (99.99%) and FAI (99.99%) were purchased from Greatcell Solar. PbI_2 was purchased from TCI. DMF (>99.8%), DMSO (>99.8%), chlorobenzene (CB, >99.8%) and diethyl ether (>99.8%) were purchased from Acros Organics. Poly[bis(4-phenyl)(2,4,6-trimethylphenyl)amine] (PTAA), C_{60} and bathocuproine (BCP) were purchased from Xi'an Polymer Light Technology. All chemicals were used as received without further purification. Solar cell substrates are pre-patterned ITO glass obtained from Yingkou Advanced Election Technology Co., Ltd.

Solar cell fabrication: ITO glass was cleaned by sequentially washing with detergent, acetone and IPA, each step for 15 min and dried by nitrogen gas. Before use, the ITO was treated with UV ozone for 30

min. PTAA (2 mg/mL in toluene) was spin-coated onto the cleaned ITO at 4000 rpm for 30 s, following with annealing at 100 °C for 10 min. The substrates were cooled down to room temperature before usage. For the composition of $FAPbI_3$ by one-step method, 1.4 M perovskite precursor solution was prepared by mixing FAI and PbI_2 in mixed solvents of DMF and DMSO (v/v = 9:1). Extra 30 mol% MACl was added to the precursor for better crystallization and phase transformation. 50 μL of the prepared precursor solution was spin-coated at 1000 rpm for 10 s and 5000 rpm for 30 s onto the PTAA-coated ITO substrate, 200 μL CB as anti-solvent was dripped on the film at 5 s before the end of the last procedure and then annealed at 150 °C for 15 min. After deposition of the perovskite active layer, 50 μL of DBNDI or DPNDI (2 mg/mL in CB) solution was spin coated on to the film at 5000 rpm for 30 s and annealed at 100°C for 5 min. Finally, 30 nm C_{60}, 5 nm bathocuproine (BCP) and 100 nm silver was evaporated sequentially.

Module fabrication: The modules connected in series were obtained by interconnects P1, P2, and P3 laser structuring. Three scribes, P1 (50 μm), P2 (150 μm), and P3 (100 μm) were etched by 1064-nm laser beam with a power of 12, 6 and 6 W, respectively. P1 line was laser-scribed on the ITO substrates. The substrates were cleaned by sequentially washing with detergent, acetone and IPA, each step for 15 min and dried by nitrogen gas. Before use, the ITO was treated with UV ozone for 30 min. After that, a PTAA layer was blade-coated onto ITO glass substrates at a speed of 15 mm/s. The gap between blade coater and ITO substrates was 100 μm. PTAA solution was prepared by dissolving PTAA in toluene with a concentration of 2 mg/ml. 1.3 M $FAPbI_3$ and 0.4 M MACl were dissolved in mixed solvent of DMF and NMP (volume ratio = 1:1). Subsequently, the precursor solution was blade-coated onto the PTAA-covered ITO glass substrates with a gap of 300 μm at a movement speed of 15 mm/s. The nitrogen knife was applied during blade coating. After that, the perovskite films were annealed at 150 °C for 15 min in 35% R.H. air. To perform surface coordinating polymerization, DBNDI or DPNDI was dissolved in CB with a concentration of 1 mg/mL and was blade-coated at a speed of 30 mm/s. with the gap of 100 μm. 30 nm C_{60} and 5 nm BCP were thermally evaporated. The deposited layers were laser-scribed for P2 line and then 100 nm sliver were thermally evaporated as electrode. Finally, the P3 line was fabricated.

Characterization: ^{207}Pb nuclear magnetic resonance (NMR) spectra were collected on a Varian Inova 400 MHz spectrometer. 0.5 M PbI_2 was dissolved in DMF, and the stoichiometry of PbI_2: NDI was 1:1 on a molar basis. Time-resolved PL spectra were measured with an Edinburgh Instruments FLS980 photoluminescence spectrometer using an EPL-635 laser pulsed at 0.5 MHz with an excitation

wavelength of 634.8 nm. The pulsed excitation fluence is 4.2 nJ/cm^2. X-ray diffraction (XRD) measurements were conducted on a Bruker D8 Discover diffractometer. X-ray photoelectron spectroscopy (XPS) measurements were performed with a ThermoFisher Ultraviolet + X-ray Photoelectron Spectrometer using a monochromatic Al K_α X-ray of 24.8 W power. An atomic force microscope (AFM, SPM SmartSPM™-1000) was employed to collected Kelvin probe force microscope (KPFM) images. Ion migration activation energies were measured and extracted following reported methods [1-3]. We used lateral devices with structures of Au/perovskite/Au with channel length of 100 μm for these measurements. The conductivity of these devices was measured by applying a 20 V bias, corresponding to an average electrical field of 0.2 V/μm, under 10^{-6} Torr vacuum on a Lake Shore tabletop cryogenic probe station with a Keithley 4200-SCS semiconductor parameter analyzer. Sample temperature was controlled in a close-circle cryostat from 150 to 350 K. We first cooled the device to 150 K and waited an hour for the temperature to stabilize. Subsequently, the device was heated and stabilized at each temperature for 10 min before current measurements were performed. To avoid transient current spikes, which occurred in the first few seconds after bias, the conductivity was extracted from the device current at 120 s after the bias was applied.

Device characterization: The *J-V* characteristics of solar cells were obtained using a Keithley 2400 source meter under simulated 1-sun AM 1.5G illumination (100mW cm^{-2}) with a solar simulator (Enlitech, SS-F5-3A) and the light intensity was calibrated by a Si photodiode. The *J-V* measurements were carried out in ambient air. The devices were measured both in reverse scan (from 1.3 to -0.2 V, step 0.01 V) and forward scan (from -0.2 to 1.3 V, step 0.01 V). The EQE was measured using an Enlitech EQE measurement system (QE-R3018).

Encapsulation and stability measurements: Devices were encapsulated in a nitrogen glovebox. PMMA (20 mg/mL in toluene) was first coated on the surface of cells. Then, Cytop was blade-coated atop PMMA. Finally, the device stacks were encapsulated using a cover glass with a UV-curable epoxy (Epoxy Technology, OG159-2) applied along its perimeter. A piece of black tape was attached to the exterior of the cover glass to protect the solar cell during UV curing. The operational stability tests were carried out at the MPPT for the encapsulated devices under AM1.5 illumination (100 mW/cm^2) in ambient air at different temperatures. For testing at 40 °C, the devices were mounted directly on the solar station. For testing at elevated temperatures, these devices were mounted on hotplates. The voltage at the MPPT was automatically applied, and the power output of the devices was tracked.

Theoretical calculations: The density function theory (DFT) calculations were implemented by using Vienna *ab*-initio simulation package (VASP) [4-6]. The Perdew-Burke-Ernzerhof (PBE) with generalized gradient approximation (GGA) was employed for the exchange-correlation functional [7]. The $FAPbI_3$ (001) surfaces were modeled using 3 × 3 slabs [8]. A plane wave basis with the cutoff energy of 400 eV and a 3 × 3 × 1 k-point mesh were used in these calculations. We consider the van der Waals (vdW) interaction using the DFT-D3 method [9]. A vacuum layer along the out-plane direction of 15 Å was constructed to restrain the interactions between adjacent slabs. The residual force and energy convergence thresholds were set to 0.02 eV $Å^{-1}$ and 10^{-4} eV, respectively.

The adsorption energy is defined as:

$$E_{ads} = E_{total} - E_{FAPbI_3} - E_{DBNDI/DPNDI}$$

where E_{total} is the total energy of the DBNDI/DPNDI adsorption interface, and E_{FAPbI_3} and $E_{DBNDI/DPNDI}$ are the energies of $FAPbI_3$ (001) surface and the DBNDI/DPNDI, respectively.

The definition formula of charge density difference is:

$$\Delta\rho = \rho_{total} - \rho_{FAPbI_3} - \rho_{DBNDI/DPNDI}$$

where ρ_{total} is the total charge density of the adsorption interface, and ρ_{FAPbI_3} and $\rho_{DBNDI/DPNDI}$ are the charge densities of the $FAPbI_3$ (001) surface and the DBNDI/DPNDI, respectively.

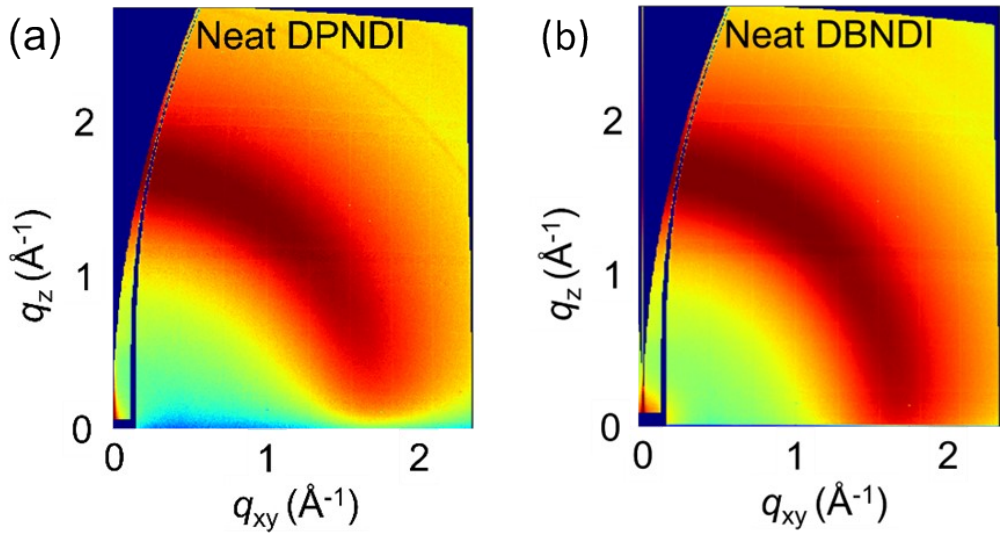

Figure S1. GIWAXS patterns of (a) neat DPNDI and (b) DBNDI films.

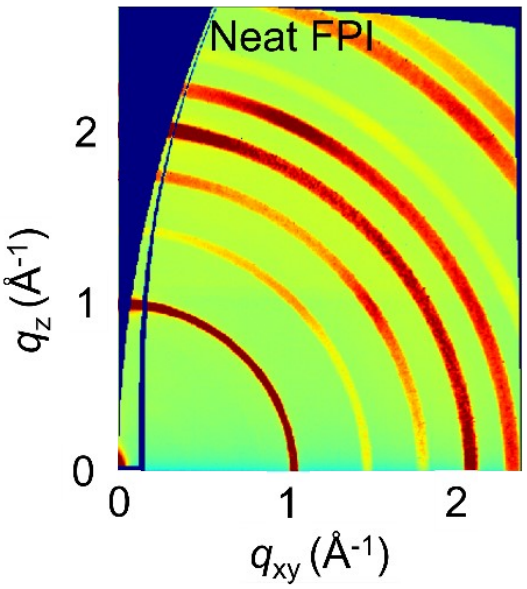

Figure S2. GIWAXS pattern of neat $FAPbI_3$ (FPI) film.

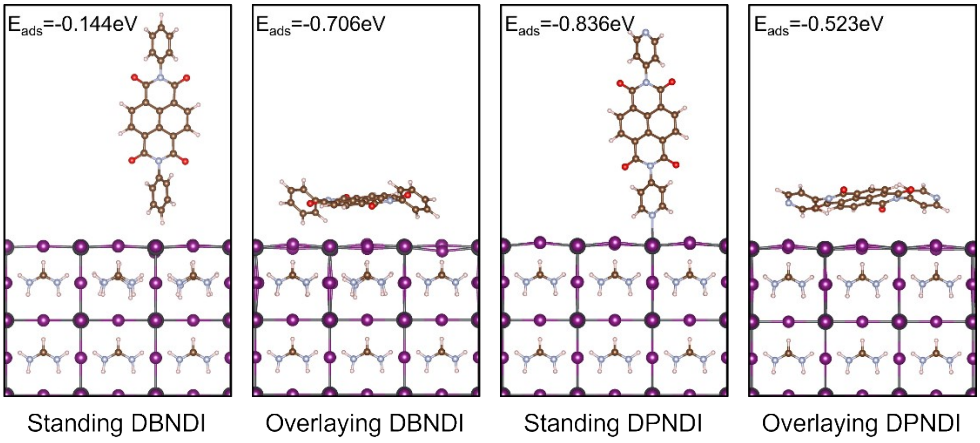

Figure S3. The adsorption structures of the DBNDI and DPNDI on $FAPbI_3$ (001) surface and their binding energies.

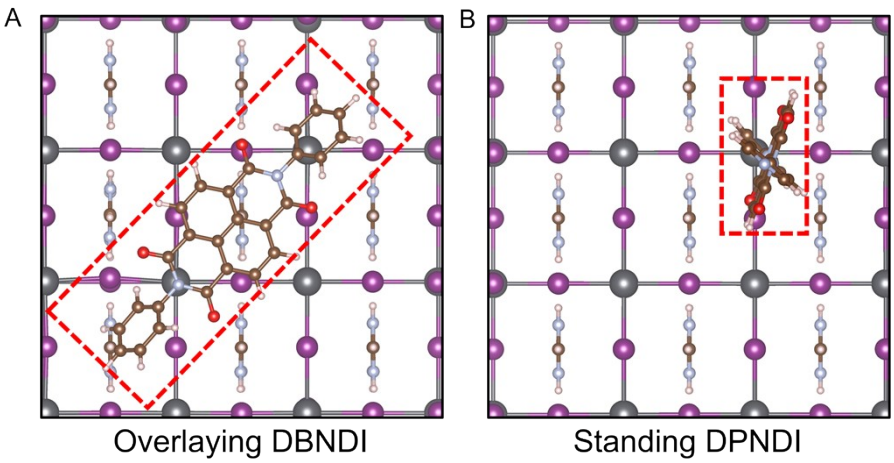

Figure S4. A top view comparison between (A) the overlaying DBNDI and (B) standing DPNDI on the FAPbI3 (001) surface, highlighting the difference in contact areas.

While the adsorption energies of overlaying DBNDI (-0.706 eV) and standing DPNDI (-0.836 eV) are comparable, the contact areas of the two groups with the perovskite surface are much different (Fig. S4). The extensive contact area of overlaying DBNDI leads to a substantial van der Waals interaction, whereas the minimal contact area of standing DPNDI results in a negligible van der Waals contribution. Consequently, the major source of adsorption energy for standing DPNDI is the formed chemical bonds, especially Pb-N coordination bonds.

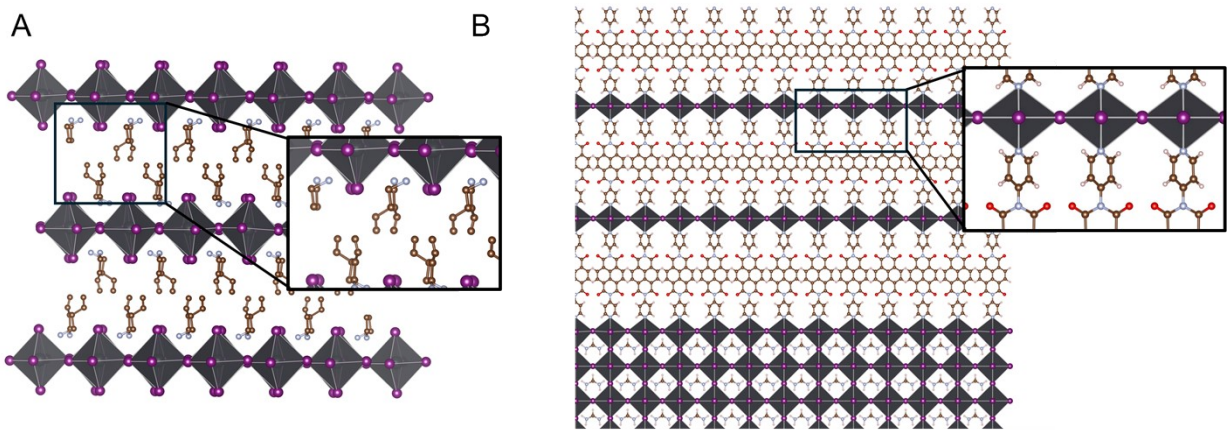

Figure S5. (A) Side view of the 2D perovskite $(BA)_2PbI_4$. (B) Side view of the 2D DPNDI(PbI_2) on the $FAPbI_3$. Inset, low angle area zoomed in.

Two-dimensional perovskites are characterized by their layered structure, composed of organic cations and inorganic frameworks. For instance, in $(BA)_2PbI_4$ (BA represents butylammonium), the organic BA^+ cations interact with adjacent PbI_2 layers via van der Waals forces (Fig. S5). However, DPNDI coordinates directly with Pb atoms through strong chemical bonds (Fig. S5B). This coordination not only mitigates the presence of excess PbI_2 but also strengthens the interfacial binding.

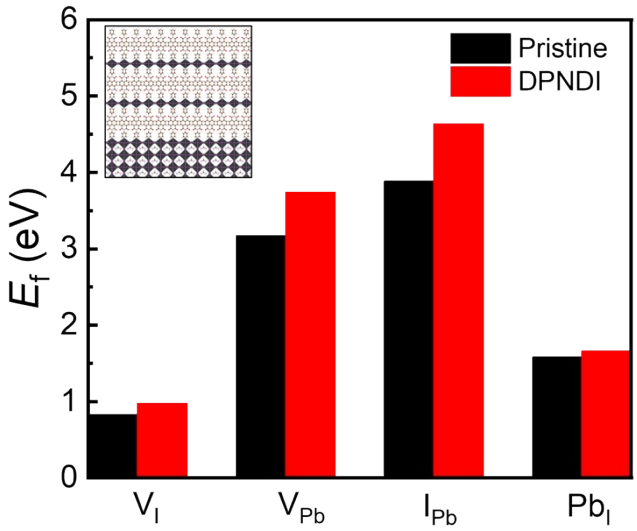

Figure S6. Defect formation energies of pristine $FAPbI_3$ and $FAPbI_3$ treated with 2D (DPNDI)PbI_2. Inset, the calculated model of 2D (DPNDI)PbI_2 on the $FAPbI_3$ film.

Except the DPNDI molecular decoration, we have also calculated the defect formation energy of 2D (DPNDI)PbI_2 covering on the $FAPbI_3$ surface (Fig. S6), and the results are consistent with our previous findings (Fig. 3D), which indicates that the DPNDI modification significantly suppresses the formation of defects.

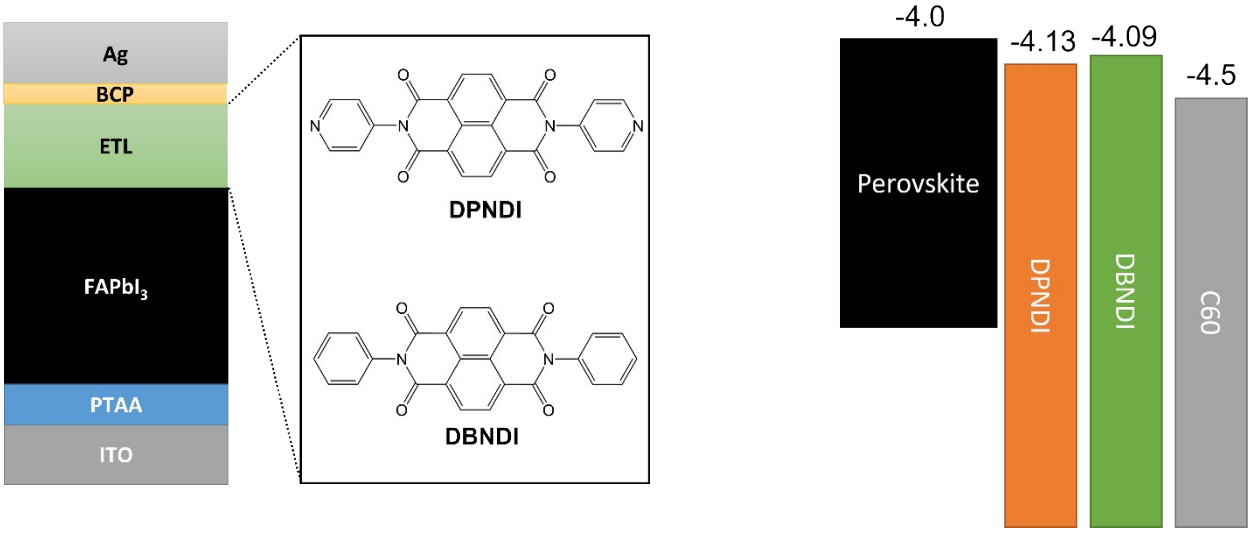

Figure S7. Energy levels of different ETL.

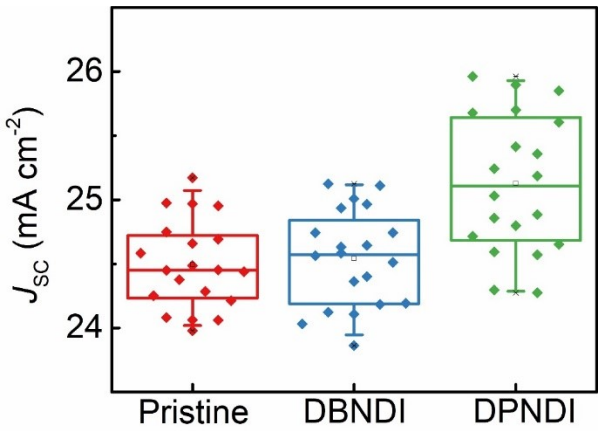

Figure S8. J_{SC} distribution of different solar cells. 20 devices were fabricated and studied in each condition.

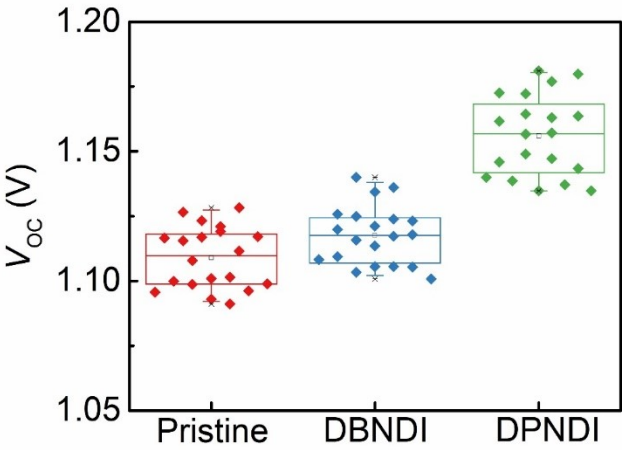

Figure S9. V_{OC} distribution of different solar cells. 20 devices were fabricated and studied in each condition.

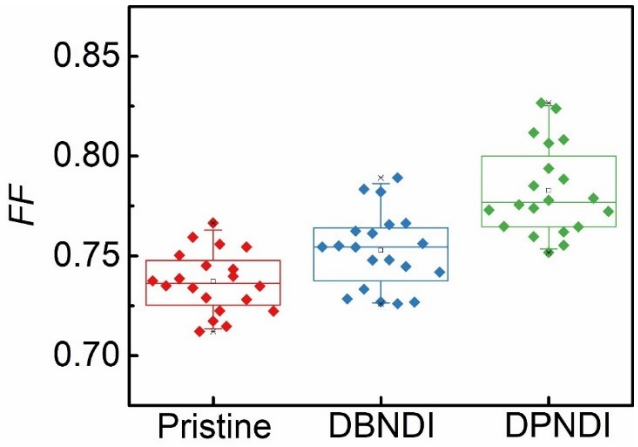

Figure S10. *FF* distribution of different solar cells. 20 devices were fabricated and studied in each condition.

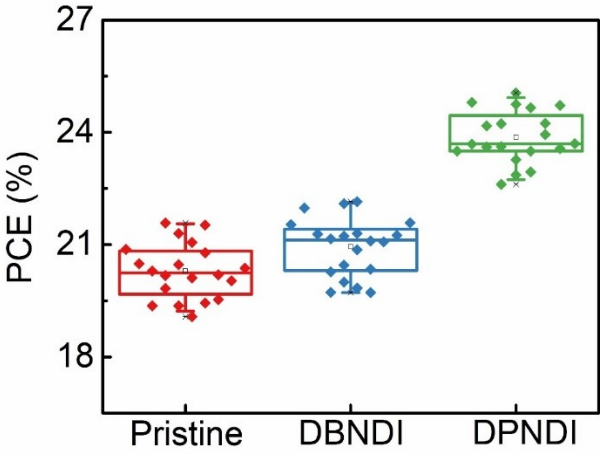

Figure S11. PCE distribution of different solar cells. 20 devices were fabricated and studied in each condition.

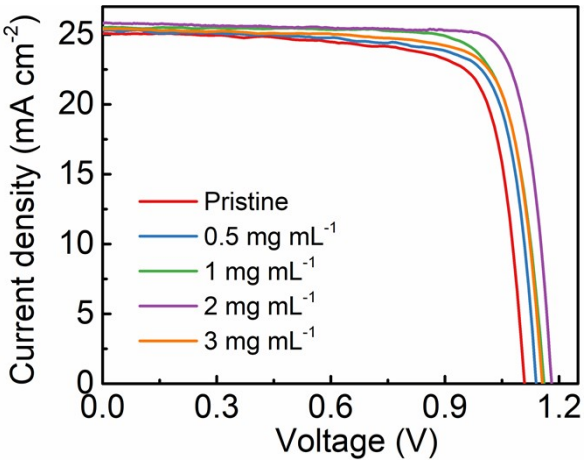

Figure S12. *J-V* characteristics of champion DPNDI PSCs with varying amounts of DPNDI.

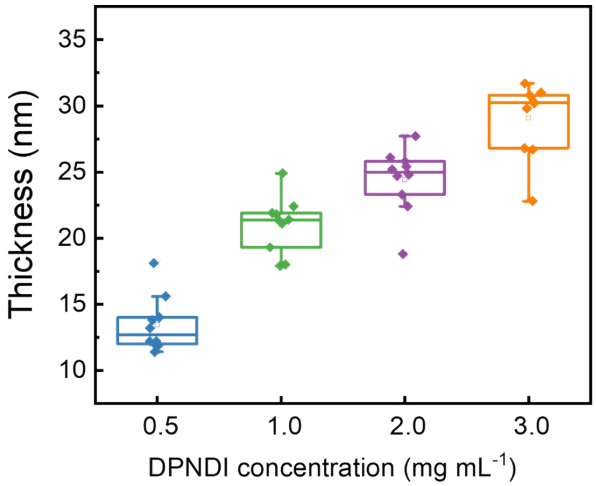

Figure S13. The thickness of the top layer with varying DPNDI concentration.

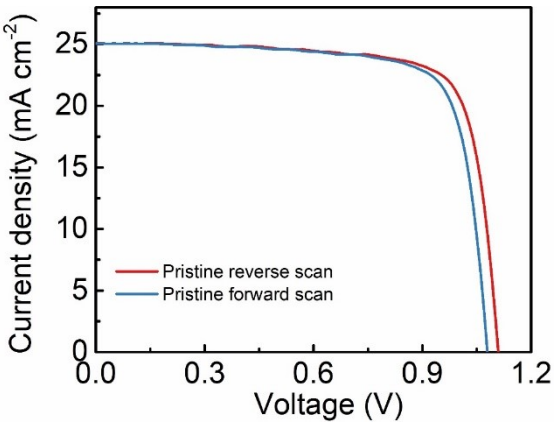

Figure S14. *J-V* characteristics of pristine PSC under different scan direction.

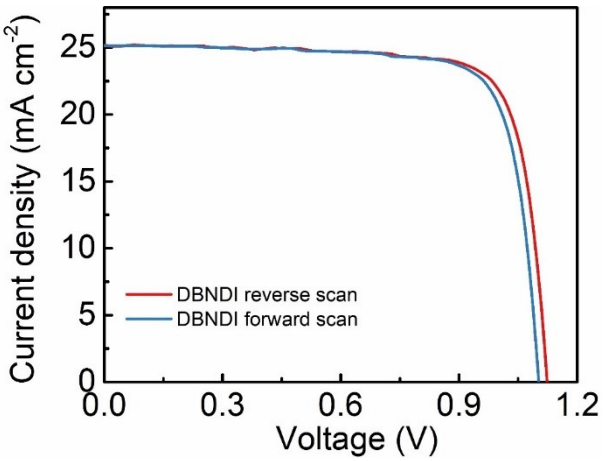

Figure S15. *J-V* characteristics of DBNDI PSC under different scan direction.

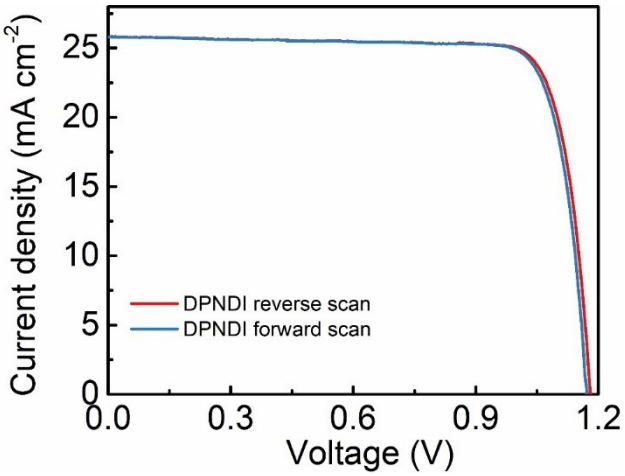

Figure S16. *J-V* characteristics of DPNDI PSC under different scan direction.

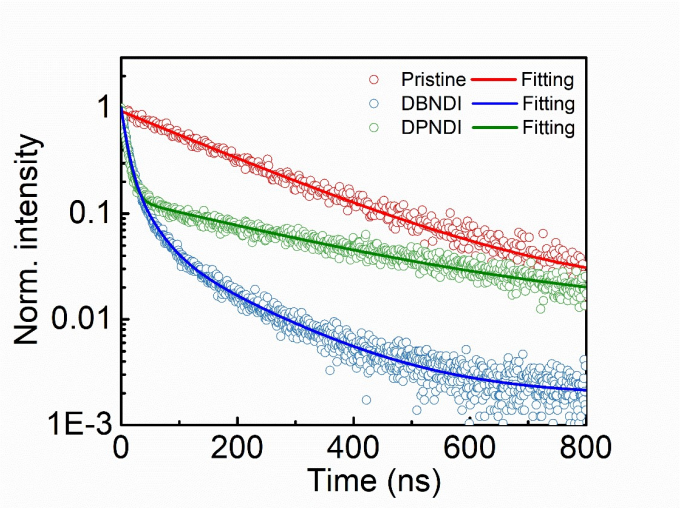

Figure S17. Time revolved photoluminescence transient spectra of stacks of glass/FPI (pristine), glass/FPI/DPNDI, or glass/FPI/DBNDI.

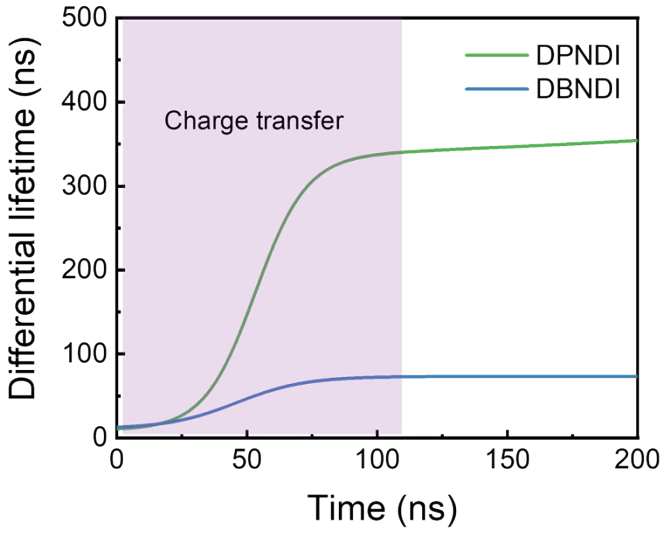

Figure S18. Differential lifetimes derived from fits to the transients in DPNDI and DBNDI treated sample.

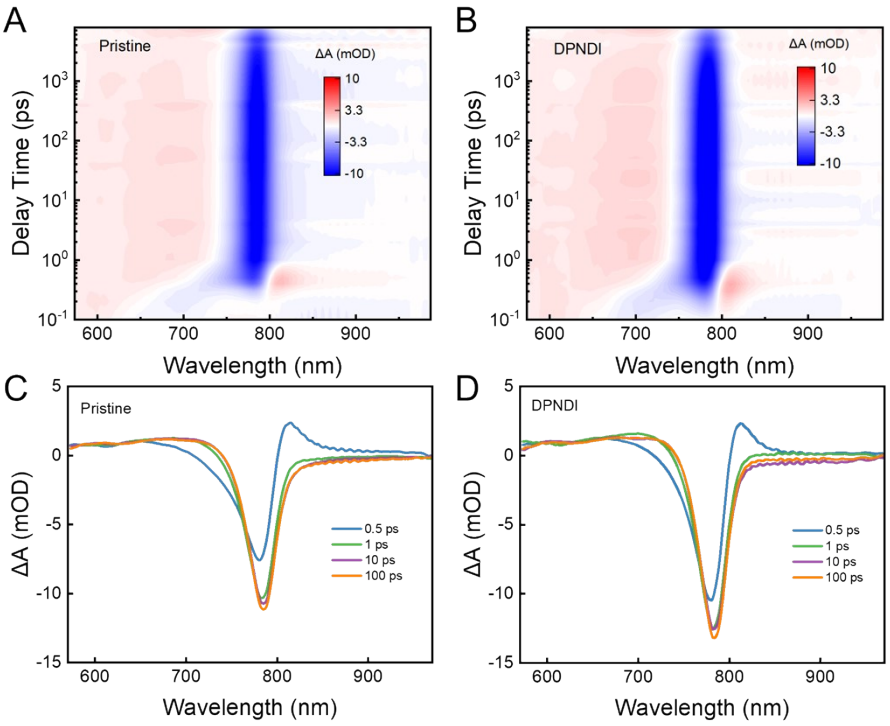

Figure S19. Ultrafast TA spectra of (A) the pristine and (B) the DPNDI-treated perovskite films. Delay time-dependent TA spectra (time scale: 0.5-100 ps) for (C) the pristine and (D) the DPNDI-treated perovskite films.

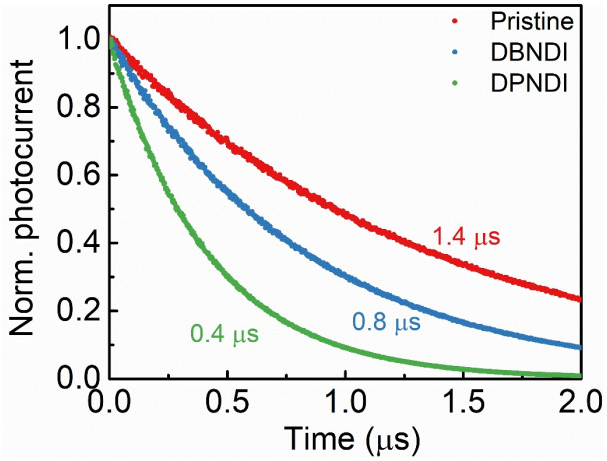

Figure S20. Transient photovoltage of pristine, DBNDI- and DPNDI-treated solar cells.

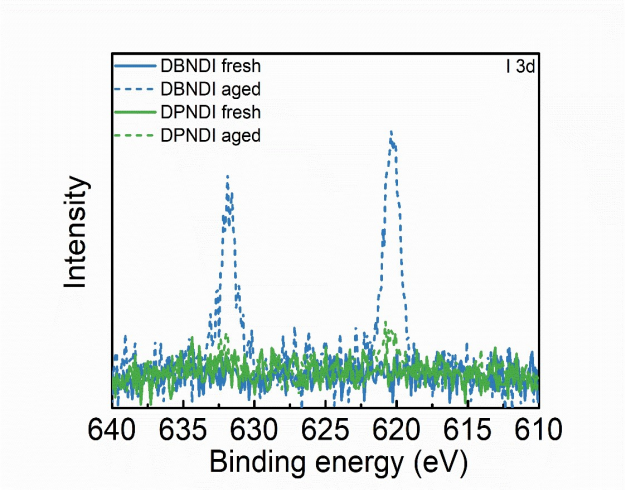

Figure S21. XPS I 3d spectra of the ETL surface in DBNDI or DPNDI modules before and after 500 hr aging. For this study, functional devices were sealed in N_2 and placed under full-sun illumination at 85 °C for the specified time before the electrodes were peeled off prior to measurement.

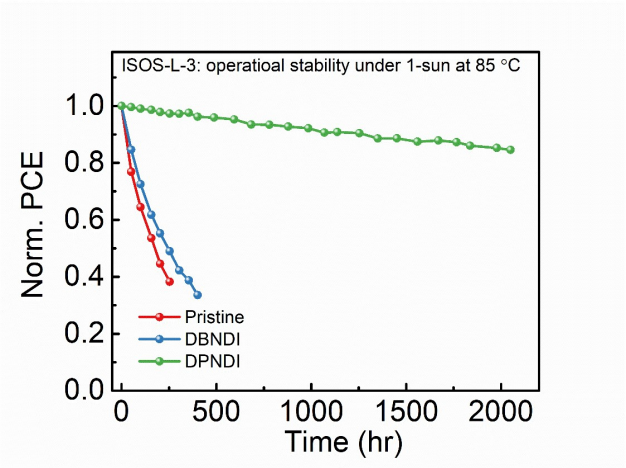

Figure S22. Normalized PCE as a function of aging time for encapsulated modules with DPNDI under constant 1-sun illumination at MPP tracking at 85 ºC in air.

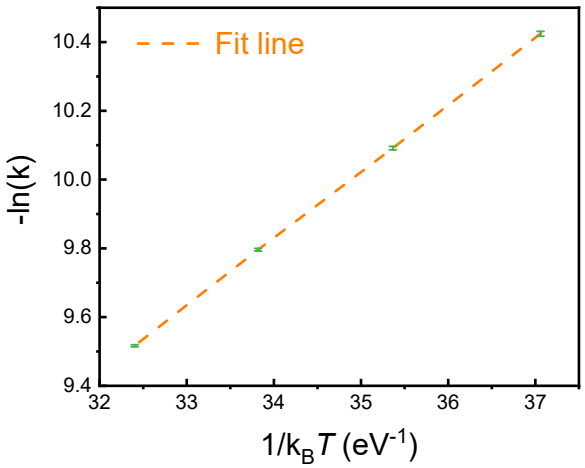

Figure S23. Natural logarithm of degradation rates k versus $1/k_{BT}$ obtained from linear fits to PCEs for capped modules, where T is the aging temperature.

Table S1. Summary of the champion and average photovoltaic parameters of control and target PSCs under reverse voltage scan. Parameters followed by * are champion device parameters. Parameters in bracket are average parameters. Average parameters are calculated based on 20 devices in each condition.

Devices	**J_{SC} (mA cm^{-2})**	**V_{OC} (V)**	**FF**	**PCE (%)**
Pristine	25.1 (24.5 ± 0.3)	1.12 (1.11 ± 0.01)	0.77 (0.74 ± 0.02)	21.6 (20.3 ± 0.7)
With DBNDI	25.1 (24.5 ± 0.4)	1.13 (1.12 ± 0.01)	0.78 (0.75 ± 0.02)	22.1 (20.9 ± 0.8)
With DPNDI	25.8 (25.1 ± 0.5)	1.18 (1.16 ± 0.02)	0.82 (0.78 ± 0.02)	25.0 (23.9 ± 0.7)
Module (31.6 cm^2 9-subcells)	2.76	10.5	0.78	22.6

Table S2. Summary of the photovoltaic parameters of the DPNDI PSCs with various amount of DPNDI.

DPNDI concentration (mg mL^{-1})	**J_{SC} (mA cm^{-2})**	**V_{OC} (V)**	**FF**	**PCE (%)**
0	25.1	1.12	0.77	21.6
0.5	25.3	1.13	0.78	22.3
1	25.5	1.16	0.79	23.4
2	25.8	1.18	0.82	25.0
3	25.4	1.15	0.78	22.8

Table S3. Recently reported efficiency and stability from perovskite solar modules. IE: initial efficiency.

Reference	Area (cm^2)	Module PCE (%)	Module stability
Joule 7, 797–809 (2023)	36.4	21.23	93% IE after 870 h (under continuous one-sun illumination)
Science 380, 404–409 (2023)	10	22.0	95% IE after 500 h (85 °C /85% RH) 90% IE after 2000 h (ISOS-L-1,at MPPT)
Science 380, 823–829 (2023)	26.9	21.8	90% IE after 2130 h (light-emitting diode (LED) light source)
Adv. Mater. 36, 2310962 (2023)	14	21.95	93% IE after 1000 h (20 °C at MPPT)
Joule 7, 1556–1573 (2023)	18	22.27	95% IE after 1000 h (85 °C /85% RH); 90% IE after 250 h (85 °C /50% RH at MPPT)
Adv. Mater. 35, 2211593（2023）	40.6	20.66	80% IE after 1040 h at MPPT
Adv. Mater. 35, 2210176（2023）	58.5	19.28	90% IE after 850 h at MPPT
Adv. Mater. 36, 2309310 (2024)	11.84	23.18	90% IE after 1184 h (≈ 0.7 sun at MPPT)
J. Am. Chem. Soc. 146, 11782–11791 (2024)	18	22.9	87% IE after 2000 h (85 °C /85% RH)
Nature Energy 9, 316–323 (2024)	31	21.1	86% IE after 1200 h (ISOS-D-3, 85% relative humidity, 85 °C)
This work	**31.6**	**22.6**	**85% IE after 2000 h (ISOS-L-3, 85 °C at MPPT)**

Reference

1. J. Xing, Q. Wang, Q. Dong, Y. Yuan, Y. Fang and J. Huang, *Phys. Chem. Chem. Phys.*, 2016, **18**, 30484-30490.
2. J. Zhao, Y. Deng, H. Wei, X. Zheng, Z. Yu, Y. Shao, J. E. Shield and J. Huang, *Sci. Adv.*, 2017, **3**, eaao5616.
3. Y. Yuan, J. Chae, Y. Shao, Q. Wang, Z. Xiao, A. Centrone and J. Huang, *Adv. Energy Mater.*, 2015, **5**, 1500615.
4. G. Kresse and J. Hafner, *Phys. Rev. B*, 1993, **47**, 558-561.
5. G. Kresse and J. Furthmuller, *Phys. Rev. B*, 1996, **54**, 11169-11186.
6. G. Kresse and D. Joubert, *Phys. Rev. B*, 1999, **59**, 1758-1775.
7. J. P. Perdew, K. Burke and M. Ernzerhof, *Phys. Rev. Lett.*, 1996, **77**, 3865-3868.
8. M. T. Weller, O. J. Weber, J. M. Frost and A. Walsh, *J. Phys. Chem. Lett.*, 2015, **6**, 3209-3212.
9. S. Grimme, J. Antony, S. Ehrlich and H. Krieg, *J. Chem. Phys.*, 2010, **132**.